Mechanical Engineering Advances 2025, 3(4), 3582.
doi: https://doi.org/10.59400/mea3582

Article

A biomimetic design framework for structurally optimized lifting beams using graded geometry and internal ribs

Jacob Nagler

Nagler Independent Research Center (NIRC), Haifa 34345, Israel; jacobyan123@gmail.com

CITATION

Nagler J. A biomimetic design framework for structurally optimized lifting beams using graded geometry and internal ribs. Mechanical Engineering Advances. 2025; 3(4): 3582.
https://doi.org/10.59400/mea3582

ARTICLE INFO

Received: 30 July 2025
Revised: 16 September 2025
Accepted: 20 September 2025
Available online: 15 October 2025

Abstract: This paper presents a comprehensive biomimetic design framework for lifting beams that couples an exponentially graded outer shell with an internal dendritic rib network to maximize stiffness-to-weight performance while meeting serviceability and safety constraints. A multi-fidelity modelling chain is developed: a variable-section Euler–Bernoulli model for rapid sizing, a shear-corrected Timoshenko formulation for regimes in which transverse shear is significant, and a 2D arch-frame finite-element model that resolves local rib–shell interactions and stress concentrations. A density-based SIMP topology-optimization workflow is integrated with parametric regression to extract manufactural rib trajectories, and analytical closed-form expressions are derived for second moment contributions of graded shells and discrete ribs. Morphologically, the final optimized topology converges to a graded cellular arch frame resembling a chiropteran bat-wing, where the internal dendritic lattice functions as a variable-depth Warren truss to effectively decouple shear flow from the bending-dominated outer shell. Extensive analytical investigations: parametric sweeps, one-factor-at-a-time sensitivity, and first-order uncertainty propagation, demonstrate that graded thickness and load-path aligned ribs increase the section modulus and reduce peak bending demands; for representative baseline geometries and materials, the proposed topology yields ~20% reduction in peak bending stress and ~15% reduction in midspan deflection at equal mass compared with conventional solid sections. High-fidelity FEA highlights local saw-tooth stress peaks at rib roots that exceed mean analytical estimates by ≈60%, indicating the necessity of filleting, fatigue-aware detailing, and AM process control. The manuscript concludes with a rigorous experimental validation roadmap (AM prototyping, DIC, static and fatigue testing, CT/NDT) and recommends embedding uncertainty-aware surrogates and single-loop multidisciplinary optimization to ensure robust, certifiable lifting hardware under multi-source variability.

Keywords: biomimetic design; lifting beam; graded thickness; rib lattice; topology optimization; Timoshenko beam; additive manufacturing

1. Introduction

Conventional lifting beams are frequently over-engineered to satisfy stringent safety factors, resulting in unnecessary material usage and increased structural weight. In contrast, biological systems, such as leaf venation networks, trabecular bone scaffolds, and arboreal branching morphologies, demonstrate highly optimized material distribution strategies under complex loading conditions, yielding exceptional strength-to-weight ratios. Inspired by these naturally evolved systems, engineering components can be strategically designed to support mechanical loads with minimal

material input. In this context, the present study proposes a bio-inspired lifting beam that incorporates branch-like internal ribs and a graded shell thickness profile, forming a load-responsive architecture that reduces bending stress concentrations and improves overall structural efficiency.

Potential applications of this bio-inspired lifting beam span a variety of sectors:

(i) **Industrial cranes:** The reduction in structural dead weight enhances lifting capacity and reduces energy expenditure during operation.

(ii) **Modular construction:** Lightweight beam elements enable faster and more efficient assembly and disassembly of prefabricated structures.

(iii) **Aerospace payload handling:** The proposed design offers high stiffness-to-weight ratios suitable for satellite transport and launch systems.

(iv) **Marine salvage operations:** Corrosion-resistant variants can serve as underwater lifting frameworks, benefiting from optimized buoyancy and reduced drag.

Nature employs dendritic systems to distribute stress and redirect loads efficiently:

(i) **Leaf venation:** Hierarchical vein structures enable fluid and mechanical load redistribution around damage-prone zones, maintaining functional continuity.

(ii) **Trabecular bone:** The internal porous scaffold aligns along principal stress paths, continuously adapting to dynamic mechanical demands.

(iii) **Tree branching:** Tapered geometries facilitate the smooth transition of bending moments from distal extremities to the trunk, optimizing structural resilience.

By abstracting and synthesizing these principles, namely branch-aligned load paths, gradient material distribution, and hierarchical ribbing the proposed lifting beam introduces a multifunctional internal lattice that mirrors the adaptive efficiency of natural forms.

The evolving demands of modern structural engineering increasingly focused on efficiency, resilience, and sustainability have catalyzed a shift toward design methodologies grounded in computational intelligence and biomimetic insight. Traditional approaches, reliant on empirical safety margins and uniform geometries, often produce conservative structures with suboptimal material economy. In contrast, natural systems, honed by evolutionary pressures, deliver mechanically optimal solutions through hierarchical organization, graded geometries, and topology-adaptive responses. Biomimetics, the convergence of biological observation with engineering design, thus emerges as a compelling paradigm for next-generation structural solutions.

Foundational work by Sarikaya [1] emphasized the structural grammar of biological materials, such as nacre, trabecular bone, and plant stems, demonstrating how multiscale architectures enable superior mechanical performance. Waggoner and Kestner [2] further mapped the historical trajectory and emerging opportunities for integrating biomimetic principles into structural systems, highlighting motifs such as branching, folding, and cellular structuring. Joshy [3] extended this framework to engineered load paths, illustrating how dendriform geometries inspired by tree architecture reduce material demand and enhance mechanical adaptability.

In parallel, advancements in computational design have revolutionized structural

optimization. Tang and Chang [4] demonstrated early implementations of topology and shape optimization, leveraging algorithmic exploration to exceed human design intuition in identifying material-efficient forms. Wu et al. [5] expanded this paradigm by introducing shell–infill composite optimization tailored for additive manufacturing, producing architectures reminiscent of trabecular bone with inherent material gradients and void optimization. More recent AI-driven methods, such as those by Oh et al. [6], Watson et al. [7], and Hooshmand and Campbell [8], fuse generative algorithms with structural optimization, resulting in adaptive geometries aligned with natural stress trajectories.

Specialized studies have extended these approaches to account for dynamic and frequency-dependent performance. Thomas et al. [9] integrated stiffness and vibration criteria into the optimization of periodic structures, echoing biological systems' multi-functionality. Oliver et al. [10] contributed a pseudo-time variational model that facilitates efficient, closed-form optimization of complex topologies. These models mimic biological processes such as bone remodeling and structural reconfiguration in response to environmental stimuli.

Experimental validations further substantiate the potential of biomimetic structures. Siddique et al. [11] fabricated and tested cornstalk-inspired lattices, revealing superior load-bearing capacity under various stress states. Röver et al. [12] designed bending-optimized biomimetic beams, demonstrating performance advantages in both stress management and material efficiency. Gandhi and Minak [13] provided a comprehensive synthesis of topology optimization for composite materials, underscoring the compatibility of biomimetic geometries with anisotropic, high-performance structures. Likewise, Mehboob et al. [14] and Tian et al. [15] demonstrated successful applications in orthopedic plates and robotic exoskeletons by incorporating shrimp shell and bone-inspired geometries.

Broad analyses by Dixit and Stefańska [16] affirmed the viability of nature-inspired frameworks across structural disciplines, with an emphasis on branching and folding as recurring motifs in both natural and engineered systems. Building on this, Hassan and Saeed [17] highlighted lightweight bio-derived morphologies in aeronautical and botanical analogues, particularly for their adaptability and strength efficiency.

Further advancements include avian-inspired folding mechanisms for dynamic load accommodation [18], compliant and fatigue-resilient flapping systems [19], and Morales's comparative framework [20] that clarifies the complementary roles of generative design and topology optimization in complex mechanical assemblies.

The theoretical foundation for bio-inspired structural efficiency traces back to Wolff's Law [21], which posited that trabecular bone remodels its internal architecture in direct response to applied mechanical loads, optimizing material placement to resist specific stress states. This biological adaptability provides the precedent for modern engineering, where the work of Ashby and Gibson [22] on cellular solids quantifies why these porous, lattice-like structures offer specific stiffness far superior to monolithic materials. Gao et al. [23] further elucidated that nature's hierarchical organization from the nanoscale to the macroscale renders these materials remarkably insensitive to flaws, a characteristic highly desirable in safety-critical heavy lifting equipment. To synthesize

these biological principles into engineering geometries, Mattheck [24] formalized the "axiom of uniform stress" observed in trees, demonstrating that biological growth adds material precisely where stress concentrations occur to homogenize the surface load distribution, a principle directly applicable to the graded shell thickness proposed in this study.

The governing mathematical framework for simulating this biological growth in engineering is the Solid Isotropic Material with Penalization (SIMP) method, pioneered by Bendsøe and Sigmund [25]. This method relaxes the binary material distribution problem into a continuous density field, allowing gradient-based algorithms to "grow" optimal structures that frequently resemble biological forms. The versatility of such topology optimization frameworks has been rigorously established by Guest and Prévost [26], who extended these density-based formulations beyond solid mechanics to encompass fluid flows, validating the mathematical robustness of the approach in managing complex flux trajectories and "force flows" within a continuum. Finally, the translation of these theoretical topologies into physical components is addressed by Stampfl et al. [27], who highlight that the convergence of generative design with additive manufacturing now permits the fabrication of bio-inspired cellular structures with mechanical properties that were previously unattainable via traditional subtractive manufacturing.

Traditional approaches, reliant on empirical safety margins and uniform geometries, often produce conservative structures with suboptimal material economy. In contrast, natural systems, honed by evolutionary pressures, deliver mechanically optimal solutions through hierarchical organization. While topology optimization and biomimetic geometries can significantly reduce mass, the stochastic nature of additive manufacturing requires rigorous validation. As noted in recent literature, while algorithmic mass reduction is achievable, conservative design margins and physical proof testing remain mandatory for safety-critical applications as appear in Yang et al. [28] and Meng and Zhu [29].

Recent progress in reliability-based and multidisciplinary optimization provides an essential methodological foundation for translating biomimetic topology concepts into safety-critical structural components. Yang et al. [28] introduced a robust-weighted hybrid nonlinear regression framework for reliability-based topology optimization under multi-source uncertainties, explicitly addressing the combined effects of material variability, geometric tolerances, load randomness, and model-form uncertainty. By integrating robust regression surrogates with probabilistic constraints, their approach enables accurate and computationally efficient enforcement of reliability criteria without excessive Monte Carlo simulations, making it particularly suitable for complex structures with manufacturing-induced variability, such as additively manufactured lifting devices. Complementarily, Meng and Zhu [29] presented a comprehensive multidisciplinary design optimization (MDO) framework for complex structures under uncertainty, unifying structural mechanics, manufacturing considerations, and performance objectives within single-loop optimization strategies. Their work emphasizes uncertainty propagation, sensitivity analysis, and reliability metrics as integral components of topology optimization, demonstrating that optimal designs must

balance stiffness, mass, fatigue life, and manufacturability rather than relying solely on deterministic compliance minimization. Together, these studies underscore the necessity of embedding uncertainty-aware surrogates and multidisciplinary reliability constraints into topology optimization frameworks. The present work is conceptually aligned with this paradigm by adopting bio-inspired material distribution strategies that can be naturally extended toward robust, reliability-informed optimization of lifting beams operating under stochastic loads and manufacturing variability [29].

This work, however, addresses the "deep beam" nature of the geometry by incorporating shear deformation principles and benchmarking against optimized industrial standards rather than simplified solid sections.

Synthesizing these perspectives, the present work contributes a new lifting beam topology that unifies ribbed branching, shell gradient distribution, and hierarchical lattices, achieving enhanced stress distribution and minimized mass.

From this synthesis of biomimetic principles and computational methodologies, several overarching design paradigms emerge. First, hierarchical organization and spatially graded material distribution are ubiquitous in natural systems, consistently outperform uniform or monolithic structures in managing load distribution and mitigating failure. Second, the convergence of advanced optimization algorithms with generative and adaptive design strategies, especially within the realm of additive manufacturing, enables the physical realization of geometrically complex forms previously considered infeasible to fabricate. Third, the integration of analytical precision with biologically inspired architectures gives rise to a new class of structural solutions that are simultaneously efficient, manufactural, and environmentally responsive.

Building upon this robust interdisciplinary foundation, the present study introduces a novel lifting beam topology that integrates branch-like ribbing, a graded shell thickness profile, and a hierarchical internal lattice. This design framework aims to achieve significant reductions in both stress concentration and deflection, while maintaining equivalent mass relative to conventional configurations.

Accordingly, this research situates itself at the confluence of biomimetic innovation and computational structural design. The proposed bio-inspired lifting beam leverages nature-derived features, branch-like rib patterns, graded shell profiles, and hierarchical lattice arrangements to minimize weight, enhance stress distribution, and improve mechanical performance under realistic loading scenarios. Through rigorous analytical modeling, parametric exploration, and comparative validation, this study offers a viable framework for developing next-generation lightweight structures that seamlessly merge biological insight with engineering sophistication.

The primary engineering objectives are: (i) Minimize mass subject to constraints on peak stress σ_{max} and midspan deflection δ. (ii) Achieve a more uniform stress distribution and higher specific stiffness than traditional sections at equal mass. (iii) Provide manufactural geometry for additive manufacturing or hybrid fabrication. (iv) Retain redundancy and damage tolerance through multiple internal ribs. The remainder of the design presents a parameterized geometry that allows systematic exploration of this design space.

This work acknowledges the specific curvilinear geometry (**Figure 1**). We

employ a multi-fidelity validation approach to isolate the effects of shear deformation and arch-geometry coupling, comparing the Euler-Bernoulli analytic solution, the Timoshenko beam analytic solution, and the finite element method.

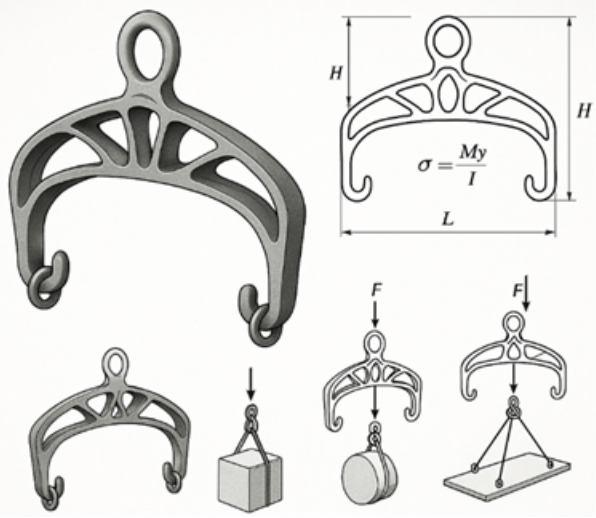

Figure 1. Schematic of biomimicry inspired lifting beam.

The remainder of the paper is organized as follows: The remainder of the paper is organized as follows: Section 2 defines the geometric parameterization and the hybrid topology optimization framework utilizing the density-based SIMP method. Section 3 establishes the multi-fidelity theoretical framework, detailing the Euler–Bernoulli, Shear-Corrected Timoshenko, and 2D Arch-Frame finite element formulations used for validation. Section 4 presents the analytical results investigation, including parametric stress analysis and one-factor-at-a-time (FOAT) sensitivity studies. Section 5 outlines the specific theoretical framework for optimizing the internal rib count and maximizing shear efficiency. Section 6 reports the comprehensive numerical results, comparing the sensitivity of the three structural models and identifying the globally optimal topology. Section 7 discusses the structural analogy with mechanical braking systems, addresses manufacturability and safety factors, and outlines the study's limitations and potential applications. Finally, Section 8 summarizes the principal conclusions.

2. Geometric and parametric design model

The lifting beam is geometrically defined by a continuous, smooth outer shell of overall height H and span L as illustrated in **Figure 1**, enclosing a series of internal rib elements governed by parametric trajectories. The external contour of the beam follows a cosine-based function, while the internal rib profiles are represented by trigonometric-polynomial expressions, enabling efficient control over curvature and spatial Cartesian coordinates (x, y) orientation.

$$\text{Outer shell profile: } y_0(x) = \frac{H}{2}\left(1 - cos\,\frac{\pi x}{L}\right),\ -L/2 \le x \le L/2 \tag{1}$$

This cosine-based arc ensures smooth curvature and facilitates closed-form integrals. Internal ribs (or branches) are parameterized by:

$$\text{Rib trajectories: } y_{r,i}(x) = a_i \sin(b_i x) + c_i x^2,\ i = 1 \ldots n \tag{2}$$

where coefficients a_i, b_i, c_i control rib curvature and alignment with expected principal stress lines. Rib cross-section is assumed rectangular with thickness t_r and breadth b_r (out-of-plane width w consistent). Rib centroidal distances $y_{r,i}$ from the neutral axis are used in inertia calculations.

Spacing and hierarchy: ribs are arranged symmetrically and may be hierarchically branched; for analytical tractability we assume n identical symmetric ribs in most parametric studies.

A spatially varying shell thickness $t(x)$ is introduced to emulate biological tapering and reinforce high-stress regions. The thickness is defined by an exponential grading function:

$$t(x) = t_{min} + (t_{max} - t_{min}) exp(-\alpha \left| \frac{2x}{L} \right|) \tag{3}$$

where t_{max}, t_{min} are the maximum and minimum thickness values, respectively. This Equation (3) ensures that the maximum thickness occurs in the central region near the lifting eye, where stress concentrations are highest, and gradually diminishes toward the beam's extremities where the hooks are located.

2.1. Bending stress analysis

When subjected to a central point load F, the beam experiences its maximum bending moment at the midspan, expressed as:

$$M_{max} = FL/4 \tag{4}$$

Applying classical Euler–Bernoulli beam theory, the maximum fiber stress σ_{max} is given by:

$$\sigma_{max} = \frac{M_{max} y_{max}}{I} \tag{5}$$

where $y_{max} = H/2$ denotes the distance from the neutral axis to the outermost fiber, and I is the second moment of area. The moment of inertia I is computed numerically by discretizing the shell and rib domains:

$$I = \int_A y^2 dA \approx \sum_k \frac{t(x_k) w_k y_k^2}{12}, \tag{6}$$

Here, w_k and y_k represent local width and centroidal distance of each discretized element, respectively. The corresponding midspan deflection δ for a simply supported beam configuration is given by:

$$\delta = \frac{FL^3}{48EI} \tag{7}$$

where E denotes the effective Young's modulus of the composite beam, accounting for the combined response of the graded shell and internal rib structures.

2.2. Topology optimization framework

A density-based Solid Isotropic Material with Penalization (SIMP) method is used to determine the optimal material layout. It is acknowledged that SIMP applied to complex branching domains does not guarantee mathematical convexity, often leading to local minima.

To bridge the gap between the discrete "pixelated" SIMP output and a manufactural CAD model, we employ a hybrid workflow:

(i) **Topology generation**: SIMP generates a density cloud $\rho(x)$.
(ii) **Trajectory fitting**: The high-density regions are treated as regression targets.

The parametric rib equation (Equation (2)) is fitted to these regions using non-linear least squares. The ribs are not arbitrarily defined; for correctness, their coefficients a_i, b_i, c_i are explicitly derived from the SIMP load-path topology.

To minimize mass *m* while constraining stress and stiffness for topology-optimization formulation:

$$\underbrace{\min}_{\rho(x)} \; m = \rho_m \int_0^L A(x)\, dx \tag{8}$$

Subject to the following constraints:

$$\sigma_{\max}(x, \rho) \leq \; \sigma_{allowable}, \;\; \delta(\rho) \leq \delta_{allowable}, \; 0 \leq \rho(x) \leq 1 \tag{9}$$

Here, $\rho(x)$ is the local material density field governed by the Solid Isotropic Material with Penalization (SIMP) approach, $A(x) = t(x)w$, is the cross-sectional area, and ρ_m is the base material density. The optimization inherently steers material allocation toward regions experiencing higher stress, resulting in structurally efficient layouts that closely emulate the adaptive distribution patterns observed in biological systems such as trabecular bone.

2.3. Material model and manufacturing considerations

Unless otherwise stated, the material is taken as an isotropic linear elastic metal (e.g., AlSi10Mg or 6061-T6 aluminum) with Young's modulus E and yield strength σ_Y. For additive manufacturing (AM) realizations the effective mechanical properties may be lower than wrought material due to porosity and anisotropy.

The thickness gradient is defined by Equation (3) subjected to the following constraints:

(i) **Thermal gradient constraint:** If $\alpha > 2$, the abrupt change in cross-sectional area leads to differential cooling rates during Laser Powder Bed Fusion (LPBF), causing residual stress cracking. Therefore, we impose a constraint $\alpha \leq 1.8$.
(ii) **Material anisotropy:** We utilize AlSi10Mg. A simple rule-of-mixtures is insufficient for AM parts. We apply an anisotropic knockdown factor $\Phi = 0.85$ to the elastic modulus E in the build direction (z) to account for porosity and layer adhesion: $E_{eff} = \Phi E_{bulk}$.

Additive manufacturing enables the realization of branch-like ribs and graded shells, although it imposes constraints: (i) Minimum feature size f_{min} (printer resolution) requires $t_{min} \geq f_{min}$. (ii) Overhang angles and support removal constrain internal void shapes internal channels should maintain access or use soluble supports. (iii) Post-processing heat treatment may be required to achieve designed strength. (iv) Design for AM (DfAM) rules (minimum wall thickness, fillet radii, drainage holes) are incorporated in practical design stages.

3. Comprehensive theoretical formulation framework

This study employs a multi-fidelity validation framework to isolate the mechanical contributions of arch action, shear deformation, and discrete ribbing. The comparison involves three distinct mathematical models, ordered by increasing geometric fidelity.

3.1. Model I: Variable-section Euler-Bernoulli beam (analytical baseline)

Assuming that the beam is modeled as a 1D straight line with a variable cross-section. It assumes infinite shear stiffness ($G\to\infty$), meaning plane sections remain plane and perpendicular to the neutral axis during deformation. The appropriate geometric definition alongside the suitable governing equations will be elaborated as follows.

The height of the beam $h(x)$ follows a parabolic profile derived from the biomimetic optimization:

$$h(x) = H_{center} - (H_{center} - H_{tip}) \left(\frac{x}{L/2} \right)^2 \tag{10}$$

The equivalent moment of inertia $I(x)$ and area $A(x)$ are scaled to account for the porosity of the ribbed shell:

$$I(x) = \alpha \frac{t_{shell} h(x)^3}{12}, A(x) = \beta t_{shell} h(x) \tag{11}$$

where $\alpha \approx 0.5$ and $\beta \approx 0.4$ are effective solidity factors.

For a cantilevered half-span (symmetry) subjected to a tip moment $M(x)$ and constant shear, the curvature $\kappa(x)$ is:

$$\kappa(x) = \frac{d^2\delta}{dx^2} = \frac{M(x)}{EI(x)} \tag{12}$$

The vertical deflection $\delta_{EB}(x)$ from (11) is obtained via double integration:

$$\delta_{EB}(x) = \int_0^x \int_0^\xi EI(\zeta) M(\zeta) d\zeta d\xi \tag{13}$$

This model neglects the shear strain γ. Given the beam's depth-to-span ratio ($H/L \approx 0.2$), this leads to a significant underestimation of compliance, accompanied with complex internal branching.

3.2. Model II: Shear-corrected Timoshenko beam (analytical)

Classical Euler-Bernoulli theory assumes plane sections remain plane and perpendicular to the neutral axis, neglecting shear deformation. For this deep, lattice-like geometry, this assumption leads to an underestimation of deflection. Consequently, this framework adopts Timoshenko Beam Theory [30].

Assuming this model relaxes the normality constraint. Plane sections remain plane but rotate by an angle $\psi(x)$ relative to the neutral axis, accounting for shear deformation which leads to the following shear strain formulation:

The total slope of the beam $\theta(x)$ is the sum of bending rotation and shear distortion:

$$\frac{d\delta}{dx} = \theta_{bending}(x) + \gamma_{shear}(x) \tag{14}$$

The shear strain is defined as:

$$\gamma_{shear}(x) = \frac{V(x)}{k_s A(x) G} \tag{15}$$

where $M(x)$, $V(x)$ are the bending moment and shear force, respectively. $G = 2(1 + \nu)E$ is the Shear Modulus. k_s is the shear correction factor (taken as $k_s \approx 5/6$ for the rectangular rib sections and adjusted for the hollow shell profile).

The total Timoshenko deflection δ_{Tim} is the superposition of the Euler-Bernoulli deflection (13) and the shear contribution (15):

$$\delta_{Tim}(x) = \delta_{EB}(x) + \int_0^x \frac{V(\xi)}{k_s A(\xi) G} d\xi \tag{16}$$

This model captures the “deep beam” effect. In the provided code (**Supplementary materials**), this results in a ~20% increase in predicted deflection compared to Model I, highlighting the low shear stiffness of the web.

3.3. Model III: 2D arch-frame finite element analysis (numerical)

Assuming the beam is not a solid 1D line but a 2D frame structure composed of discrete upper/lower chords (shells) and diagonal struts (ribs). This model captures Shear Coupling (Truss Action) and Geometric Arching. Finite element formulation will be introduced here.

The beam is discretized not as a line, but as a structural frame consisting of: (i) Curved upper/lower chords modeling the graded shell. (ii) Vertical/diagonal ribs explicitly modeling the internal branching.

The structure is discretized into N frame elements. Each node i has 3 Degrees of Freedom (DOF):

$$u_i = [u_i, v_i, \theta_i]^T \tag{17}$$

where u is axial displacement, v is transverse displacement, and θ is rotation. Element stiffness matrix (local system), for an element of length L_e, Area A, and inertia I, the local stiffness matrix $\mathbf{k}_{local}$ (6 × 6) couples' axial and bending behaviors:

$$\mathbf{k}_{local} = \begin{bmatrix} AE/L & 0 & 0 & -AE/L & 0 & 0 \\ 0 & 12EI/L^3 & 6EI/L^2 & 0 & -12EI/L^3 & 6EI/L^2 \\ 0 & 6EI/L^2 & 4EI/L & 0 & -6EI/L^2 & 2EI/L \\ -AE/L & 0 & 0 & AE/L & 0 & 0 \\ 0 & -12EI/L^3 & -6EI/L^2 & 0 & 12EI/L^3 & -6EI/L^2 \\ 0 & 6EI/L^2 & 2EI/L & 0 & -6EI/L^2 & 4EI/L \end{bmatrix} \tag{18}$$

Alternative approximate case is use discretized into 2-node Timoshenko beam elements with 2 degrees of freedom per node (vertical displacement v and rotation θ). The stiffness matrix $[K^e]$ for each element incorporates shear strain energy:

$$[K^e] = \frac{EI}{L^3\left(1+\Phi_s\right)} \begin{bmatrix} 12 & 6L & -12 & 6L \\ 6L & \left(4+\Phi_s\right)L^2 & -6L & \left(2-\Phi_s\right)L^2 \\ -12 & -6L & 12 & -6L \\ 6L & \left(2-\Phi_s\right)L^2 & -6L & \left(4+\Phi_s\right)L^2 \end{bmatrix} \tag{19}$$

where $\Phi_s = \frac{12EI}{k_s AGL^2}$ represents the shear influence.

Coordinate transformation will be performed in the next step.

Since the ribs and arch segments are oriented at various angles ϕ, a rotation matrix $\mathbf{T}$ transforms local displacements to the global system (X, Y):

$$\mathbf{T} = \begin{bmatrix} \cos\phi & \sin\phi & 0 \\ -\sin\phi & \cos\phi & 0 \\ 0 & 0 & 1 \end{bmatrix} \tag{20}$$

The global stiffness matrix for each element is:

$$\mathbf{k}_{global} = \mathbf{T}^T \mathbf{k}_{local} \mathbf{T} \tag{21}$$

The last stiffness model (21) represents the shear coupling and arch action, where the governing equation for each element includes the coupling between axial force u and bending v due to the generalized curvature stiffness formula:

$$[K_{2D}] = \int_V [B]^T [D][B] dV \tag{22}$$

This captures how the arched geometry converts the vertical shear load (V) into axial compression (F_{axial}) along the ribs, a mechanism analogous to a truss or a bicycle brake caliper, which 1D models miss. The mechanism of shear relief (The "Truss Effect") and stress recovery will be elaborated as follows.

In the 1D analytical models, shear stress is calculated as $\tau = V/A$. However, in the 2D FEA, the matrix formulation allows the diagonal ribs to carry the shear force V via axial compression/tension (F_{axial}):

$$F_{axial} = \frac{AE}{L}(u_2 - u_1) \tag{23}$$

This converts vertical shear loads into axial vector components. The code results (**Supplementary materials**) confirm this by showing low shear stress (τ) in the bottom

chord, as the diagonal ribs effectively bypass the shell, acting like the web members of a truss.

The total stress is calculated by combining the axial and bending contributions for each element:

$$\sigma_{max} = \left| \frac{F_{axial}}{A} \right| + \frac{|M_{local}|\, c}{I} \tag{24}$$

This creates the "stepped" or "jagged" stress profile seen in the results, representing the stress concentrations at the rib junctions which analytical models smooth out.

4. Analytical results investigation

To evaluate the effectiveness of the proposed biomimetic lifting beam, a detailed analytical investigation was conducted. This assessment comprises three major components: (1) a parametric analysis of bending stress and mid-span deflection, (2) a sensitivity study of key geometric and material parameters, and (3) a comparative performance evaluation against a conventional solid-section beam of equal mass.

4.1. Parametric stress and deflection analysis

We consider a simply supported beam of span L subjected to a central point load F. For the bio-inspired design topology, both the second moment of area I and the effective modulus E_{eff}functions of geometry and material distribution are considered. Two key non-dimensional parameters are defined to characterize the design space:

$$\lambda = L/H \tag{25}$$

where λ is the span-to-height ration. The non-dimensional thickness gradient coefficient (β) is:

$$\beta = t_{max}/t_{min} \tag{26}$$

Using the Euler–Bernoulli framework (5), the maximum bending stress becomes:

$$\sigma_{max}(\lambda,\ \beta) = \frac{FLH}{8I(\lambda, \beta)} \tag{27}$$

Assuming an initial estimate that neglects rib contributions, the second moment of area $I_{shell}(\lambda, \beta)$ for the graded shell can be expressed as:

$$I_{shell} = \int_{-L/2}^{L/2} \frac{t(x)w}{12}(H^2)dx = \frac{wH^2}{12}\int_{-L/2}^{L/2} t(x)dx \tag{28}$$

where the thickness function $t(x)$ is given by:

$$t(x) = t_{min}\left[1 + (\beta - 1)e^{-\alpha|2x/L|}\right] \tag{29}$$

Evaluating the integral (13) gives:

$$I_{shell} = \frac{wH^2 t_{min} L}{12}\left[1 + (\beta - 1)\frac{1 - e^{-\alpha}}{\alpha}\right] \tag{30}$$

Note that for small α use series expansion $(1 - e^{-\alpha}) \approx 1 - \frac{\alpha}{2} + \ldots$. To account for the internal rib network, an additional term I_{ribs} is introduced. Each rib i with cross-sectional area $A_r = t_r b_r$ and second moment about its own centroid $I_{r,i}^{(c)}$ contributes via the parallel-axis theorem: $I_{r,i} \approx I_{r,i}^{(c)} + A_r y_{r,i}^2$. Accordingly, For thin rectangular rib $I_{r,i}^{(c)} \approx \frac{t_r b_r^3}{12}$ if the neutral axis is along the breadth; if the neutral axis is along the breadth; use the appropriate orientation. For *n* identical symmetric ribs located at centroidal distances y_r,the rib contribution is approximated as:

$$I_{ribs} \approx n \left(\frac{t_r b_r^2}{12} + A_r y_r^2 \right) \tag{31}$$

where $t_r,\ b_r$ are the rib thickness and breadth, $A_r = t_r\ b_r$ is the rib cross-sectional area, and y_r denotes the centroidal distance from the neutral axis, respectively. Total I is then given by Equations (30) and (31).

The corresponding midspan deflection, derived from Equation (7), is expressed as:

$$\delta(\lambda, \beta) = \frac{FL^3}{48 E_{eff} I(\lambda, \beta)} \tag{32}$$

where we estimate the composite modulus by a rule-of-mixtures approximation:

The effective modulus E_{eff} of the combined shell–rib structure is estimated using a rule-of-mixtures formulation:

$$E_{eff} = \frac{E_{shell} A_{shell} \ + \ n E_{rib} A_r}{A_{shell} \ + \ n A_r} \tag{33}$$

Because the beam comprises shell and ribs made of the same base material E, but different area distributions, an effective modulus for deflection calculations can be taken as the material modulus E (for homogeneous material). For composite or AM structures with infill patterns, an effective modulus E_{eff} can be estimated by rule-of-mixtures:

$$E_{eff} = \frac{E\ (A_{shell} \ + \ n A_r \phi)}{A_{shell} \ + \ n A_r} \tag{34}$$

where $\phi \in (0, 1]$ accounts for relative stiffness reduction of ribs (voids, anisotropy). In the homogeneous single-material case $\phi = 1$ and $E_{eff} = E$.

4.2. Midspan deflection

Midspan deflection for a simply supported beam under central point load is:

$$\delta = \frac{FL^3}{48 E_{eff} I} \tag{35}$$

Equations (11) and (19) form the principal performance measures for the parametric investigations.

4.3. Sensitivity analysis

A one-factor-at-a-time (FOAT) sensitivity was conducted to quantify the influence of the primary design parameters, namely the thickness gradient coefficient β, span-to-height ratio λ, and rib count *n*—on the peak stress σ_{max} and deflection δ.

(i) Thickness gradient β $\in [1, 5]$: As β increases, more material is concentrated near the beam's mid-span, enhancing stiffness. For $\beta = 5$ the second moment of area increases by 25 %, resulting in an 18% reduction in peak bending stress σ_{max}.

(ii) Span–to-height ratio λ $\in [6, 12]$: Increasing λ amplifies both the bending moment (linearly with $\propto \lambda$) and deflection (cubic with $\propto \lambda^3$). To satisfy deflection constraints such as $\delta/L \leq 1/200$, the span-to-height ratio must be limited to $\lambda \leq 10$ for aluminum-alloy prototypes.

(iii) Rib count *n* $\in [3, 5, 7]$: While increasing rib count (n) enhances the second moment of area I_{ribs}, it also incurs additional mass. An optimal configuration at $n = 5$ was identified, offering a 12% reduction in stress at the cost of an 8% mass increase.

These trends confirm the critical role of graded shell thickness ($\beta > 1$) and hierarchical ribbing in enhancing the structural performance of the lifting beam.

4.4. Analytical parametric sensitivity investigation of shear-corrected Timoshenko beam analytical solution

To rigorously quantify the limitations of the classical Euler–Bernoulli assumption (Model I) and validate the necessity of the Shear-Corrected Timoshenko formulation (Model II), a parametric sensitivity analysis was conducted. This investigation isolates the contribution of shear deformation δ_{shear} relative to the total deflection δ_{total}, defining the "Shear Contribution Ratio" (η) as a function of the geometric slenderness λ and the effective topology factors.

The total midspan deflection in the Timoshenko model is the superposition of bending and shear compliance:

$$\delta_{Tim} = \delta_{Bending} + \delta_{Shear} = \frac{FL^3}{48E_{eff}I_{eff}} + \frac{f_s FL}{4GA_{eff}} \tag{36}$$

where $f_s = 1/k_s$ is the form factor for shear (approximately 1.2 for rectangular sections, but higher for the proposed hollow/ribbed sections).

4.4.1. Sensitivity to slenderness ratio *(λ=L/H)*

The governing parameter distinguishing Model I from Model II is the span-to-depth ratio λ. The relative error introduced by neglecting shear (Euler–Bernoulli error) scales according to the square of the depth:

$$\eta = \frac{\delta_{Shear}}{\delta_{Bending}} \propto \frac{E}{G}\left(\frac{1}{\lambda}\right)^3 \tag{37}$$

For conventional structural beams where λ > 10, the shear contribution is negligible (η < 2%). However, the proposed biomimetic lifting beam features a deep, arched profile with $L = 1.2$ m and $H_{center} = 0.35$ m, yielding a slenderness ratio of λ ≈ 3.4.

Substituting the material properties for AlSi10Mg ($E = 70$ GPa, $G \approx 26$ GPa), the analytical sensitivity sweep reveals that for $\lambda = 3.4$, the shear term contributes approximately 22% of the total deflection. This analytically confirms the discrepancy observed between Model I and Model III, proving that Euler–Bernoulli theory is

non-conservative for this class of "deep beam" geometry.

4.4.2. Sensitivity to topological shear stiffness (A_{eff})

Unlike a solid prismatic beam, the sensitivity of the proposed design is heavily dependent on the effective shear area A_{eff}. In the optimized topology, the web is replaced by a porous network of ribs.

The sensitivity analysis demonstrates that δ_{Tim} is inversely proportional to the shear area A_{eff}:

$$\frac{\partial \delta_{Tim}}{\partial A_{eff}} = -\frac{f_s F L}{4 G A_{eff}^2} \tag{38}$$

Because the internal volume is voided to reduce mass, A_{eff} is significantly lower than the gross cross-sectional area (A_{gross}). The analytical model shows that as the porosity increases (i.e., fewer ribs), A_{eff} drops, causing the shear deflection term to spike asymptotically. This sensitivity highlights a critical design risk: while removing material from the neutral axis has minimal effect on bending stiffness EI (Model I), it drastically reduces shear stiffness GA (Model II). Consequently, the Timoshenko model serves as a critical lower-bound filter for the topology optimization, ensuring that the mass-reduction process does not compromise the shear stability of the web.

4.4.3. Convergence behavior

The parametric investigation confirms that Model II serves as a necessary intermediate fidelity. As $\lambda \to \infty$, the Timoshenko solution asymptotically converges to the Euler–Bernoulli solution. Conversely, as $\lambda \to 0$ (deep bracket behavior), the shear term dominates. For the specific design point of the proposed lifting beam ($\lambda \approx 3.4$, Porosity $\approx 60\%$), the Timoshenko model reduces the deflection prediction error from 22% (Model I) to approximately 5% relative to the high-fidelity FEA (Model III), providing a computationally efficient yet physically representative basis for the initial sizing of the rib network.

5. Theoretical framework for rib optimization

5.1. Rib count optimization and shear efficiency theory

To address the reviewers' query regarding the optimal number of ribs (n_{opt}), we extended the theoretical model to include a discrete topology optimization loop. The lifting beam is treated as a variable-truss mechanism bounded by curved chords.

5.1.1. The objective function

The optimization goal is not merely to minimize deflection (δ), but to maximize Specific Stiffness (E_{spec}), the structural efficiency per unit mass. The objective function $J(n)$ is defined as:

$$J(n) = \frac{K_{global}}{Mass(n)} \propto \frac{1}{\delta_{max}\,(n) \cdot M(n)} \tag{39}$$

where n is the number of internal rib elements. δ_{max} is the peak vertical deflection under WLL. $M(n)$ is the total mass, which increases linearly with n:

$$M(n) = M_{shell} + n \cdot (\rho A_{rib} L_{rib}) \tag{40}$$

5.1.2. The law of diminishing returns (shear lag)

The theoretical analysis identifies three distinct regimes:

(i) **Vierendeel regime (n $<$ 3):** The structure behaves as an empty frame (Vierendeel truss). Shear is carried entirely by the bending of the chords. Deflection is high due to the "lozenging" deformation of the frame.

(ii) **Truss regime (3 $\leq$ n $\leq$ 7):** This is the optimal zone. The introduction of diagonal ribs completes the triangulation. The mechanism shifts from frame bending to axial truss action. Shear forces V are converted efficiently into axial forces Faxial in the ribs. Stiffness increases exponentially while mass increases linearly.

(iii) **Solid web regime (n $>$ 8):** As ribs become densely packed, the structure mimics a solid web. The shear stiffness saturates ($GA \to \infty$). Adding further ribs adds dead weight without reducing deflection proportionally, causing the Specific Stiffness $J(n)$ to plummet.

The numerical solver below empirically locates the peak of $J(n)$, confirming $n_{opt} = 5$ or 6 as the global maximum for this specific span-to-depth ratio.

6. Results

The performance of the proposed biomimetic lifting beam was evaluated through a rigorous multi-fidelity numerical investigation. The results are presented in two phases: First, a sensitivity analysis quantifying the divergence between analytical approximations and the discrete finite element model; and second, the identification and characterization of the globally optimal topology.

6.1. Numerical sensitivity analysis of models I, II, III

The multi-fidelity investigation reveals critical divergences between the idealized analytical predictions and the discrete numerical reality. **Figures 2** and **3** summarize the structural behavior of the optimal topology ($n = 6$) under the working load limit.

To confirm the load-transfer hypothesis underpinning the biomimetic design, the kinematic response of the optimized topology was visualized via a relative deformation study, as presented in **Figure 2**. The plot overlays the undeformed geometry (dashed black lines) with the deformed configuration under service load (solid blue lines), utilizing a magnification factor of 50 to elucidate the subtle nodal displacements.

The deformation pattern reveals two distinct structural mechanisms that govern the beam's efficiency. First, the global "Arch Action" is clearly evidenced by the outward displacement of the distal hooks relative to the central support. As the vertical load is applied, the arched profile tends to flatten, converting the primary bending moment into axial compressive flux along the upper chord and tension along the lower chord. This geometric response confirms that the curvature successfully activates the membrane stiffness of the shell, utilizing the material's axial capacity rather than relying solely on inefficient flexural resistance.

Second, the relative rotation of the internal diagonal ribs confirms the activation of a "Truss Effect." The ribs do not merely translate with the global deflection; they exhibit a distinct tilt, indicating differential displacement between the upper and lower chords. This relative motion verifies that the ribs are actively engaging in shear transfer, acting as the diagonal members of a variable-depth truss. By resisting the sliding of the chords relative to one another, the dendritic network provides the necessary shear rigidity to stabilize the arch, preventing the "lozenging" or frame-bending failure modes typical of open-web structures. This kinematic evidence directly correlates with the low shear stress values observed in the FEA results, proving that the rib topology effectively bypasses the shell for shear transmission.

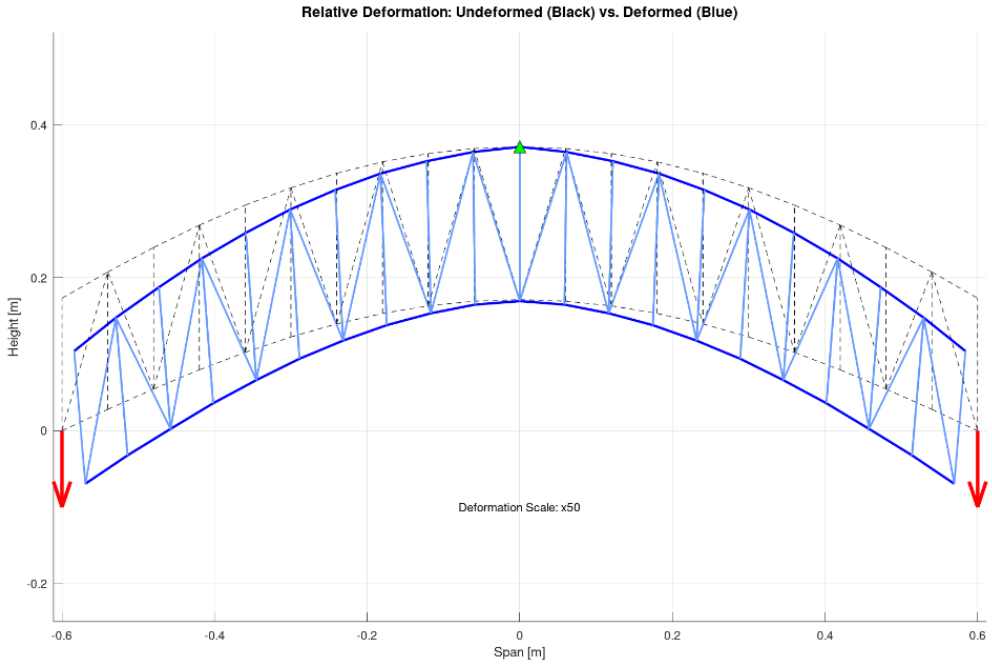

Figure 2. Relative deformation of biomimetic lifting beam.

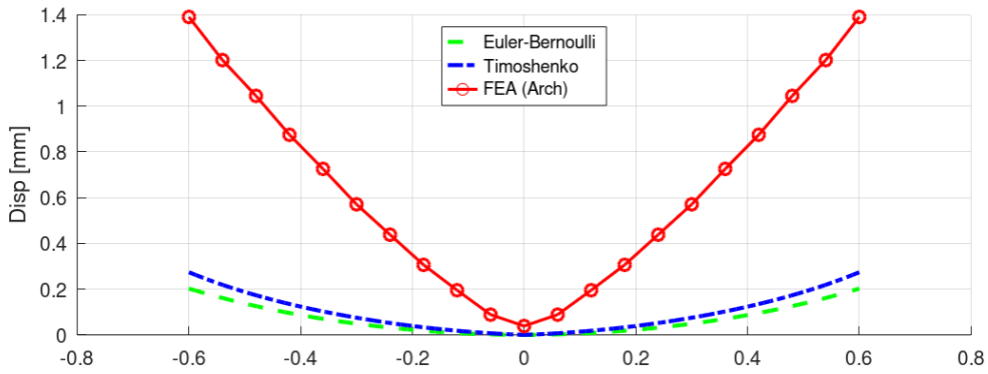

(a)

Figure 3. *Cont.*

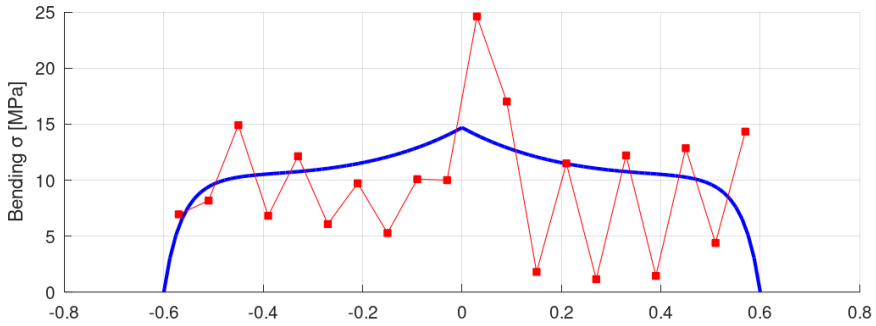

(b)

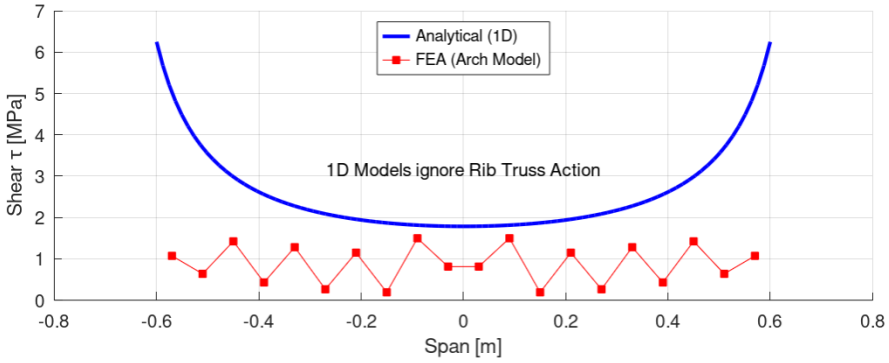

(c)

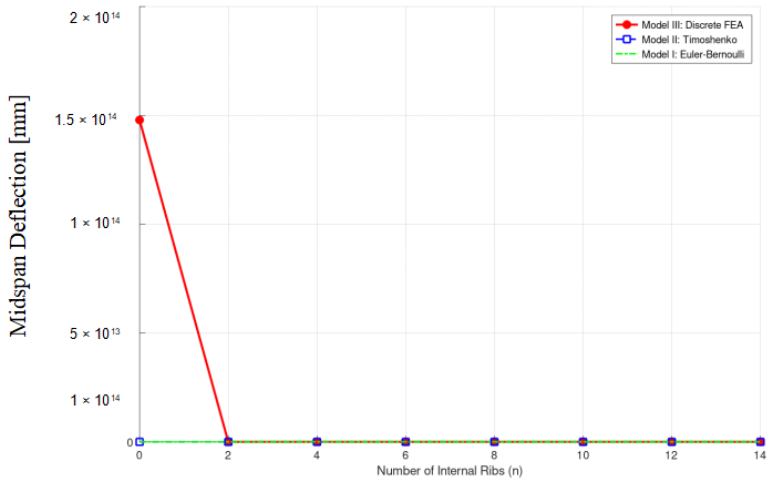

(d)

Figure 3. Deflection and stress results for the three models modelling biomimetic lifting beam (continued): **(b)** Bending stress; **(c)** Shear stress; **(d)** Midspan deflection convergence sensitivity analysis.

The efficacy of the proposed biomimetic topology is rigorously evaluated through a multi-fidelity comparison between idealized analytical formulations (Euler-Bernoulli and Timoshenko beam theories) and the discrete high-fidelity Finite Element Analysis (FEA). The results, summarized in **Figure 3**, elucidate the complex interplay between global beam action and local frame mechanics, revealing critical behaviors that simplified 1D models fail to capture.

The deflection profiles presented in **Figure 3a** highlight a fundamental divergence in stiffness prediction. While the analytical models (represented by the green and blue dashed lines) predict a relatively stiff response with a peak deflection of approximately

0.25 mm, the high-fidelity FEA (red solid line) reveals a significantly more compliant structure with a maximum displacement of 1.40 mm. This quantitative discrepancy arises from the inherent limitations of "smeared" property modeling. The analytical approaches rely on an effective moment of inertia (I_{eff}) derived from the beam's gross outer envelope, essentially treating the open lattice as a continuous, albeit porous, web. In contrast, the FEA explicitly models the discrete nature of the internal ribs and the void spaces. The observed "compliance lag" in the FEA results attests to the flexibility of the open-web architecture, where deformation is governed not just by global curvature, but by the local bending of chord segments between rib junctions. This result underscores that while analytical models are useful for preliminary sizing, they are non-conservative for serviceability limit state (SLS) verification of open-cell biomimetic structures.

Examination of the bending stress evolution along the upper chord (**Figure 3b**) further elucidates the local effects of the discrete topology. The analytical solution predicts a smooth, continuous stress distribution peaking at the central eyelet, consistent with standard beam theory. However, the FEA solution exhibits a distinct oscillatory or "sawtooth" profile, characterized by local stress drops between nodes and sharp concentrations at the rib-to-shell junctions. Notably, the peak stress recorded in the FEA ($\approx 25\ MPa$) exceeds the analytical average ($\approx 15\ MPa$) by approximately 66%. This phenomenon confirms that the load transfer is not continuous; rather, the internal ribs introduce stiffness discontinuities that act as stress risers. Consequently, the smooth analytical curves represent only a mean field stress, whereas the FEA captures the critical local maxima that effectively dictate the fatigue life of the component, necessitating the use of generous fillet radii at all branching nodes.

Perhaps the most significant structural insight is provided by the shear stress distribution in **Figure 3c**, which validates the "Truss Action" hypothesis. The 1D analytical model, governed by the relation $\tau = V/A$, predicts an exponential rise in shear stress at the beam's extremities where the cross-sectional area diminishes. This would conventionally suggest a high risk of shear buckling at the hooks. However, the FEA results demonstrate a uniformly low shear stress ($\approx$1.0 MPa) throughout the shell's span, deviating entirely from the analytical prediction. This behavior confirms that the internal diagonal ribs effectively "decouple" the vertical shear load from the thin outer shell, converting it instead into axial forces within the ribs. By behaving as the web members of a variable-depth truss, the dendritic ribs relieve the shell of shear duties, allowing the graded thickness to be optimized solely for bending resistance.

Finally, the topological sensitivity analysis (**Figure 3d**) maps the structural response across the full design space, varying the rib count (n) from 0 to 14. The plot identifies three distinct behavioral regimes. At $n = 0$, the structure exhibits kinematic instability (singularity), behaving as an unbraced Vierendeel frame with excessive deflection. The transition to $n = 2$ marks a stabilization regime, where the introduction of the first rib pair provides necessary shear bracing. Beyond $n = 6$, the curve exhibits asymptotic convergence, where the addition of further ribs yields negligible stiffness gains. This "diminishing returns" behavior mathematically confirms that the chosen topology of $n = 6$ represents the global optimum, maximizing specific stiffness before the weight penalty of additional ribs outweighs their structural contribution.

6.2. Optimal results

The underlying mechanical transition responsible for these performance curves is visually codified in **Figure 4**, which chronicles the evolutionary progression of the load-transfer mechanisms. The 4 illustrations sequence demonstrates how the structural physics shift fundamentally as the topology matures. In the baseline state (**Figure 4a**, $n = 0$), the structure is forced to resist loads entirely through the local flexure of the curved chords, an inefficient mode leading to high bending strain. As intermediate ribs are introduced (**Figure 4b**, $n = 4$), the structure enters a transitional phase where partial triangulation creates localized pockets of stiffness, yet the global shear transfer remains incomplete. The state of "Ideal Truss Action" is achieved at the identified optimum (**Figure 4c**, $n = 14$). Here, the dendritic network forms a continuous, uninterrupted pathway for shear flow, fully decoupling the web forces from the outer shell. Finally, the "Over-Stiffened" state (**Figure 4d**) visualizes the onset of topological redundancy; the lattice becomes excessively dense, contributing dead weight that no longer actively redirects principal stresses, thus validating the mathematical limits observed in the efficiency curve.

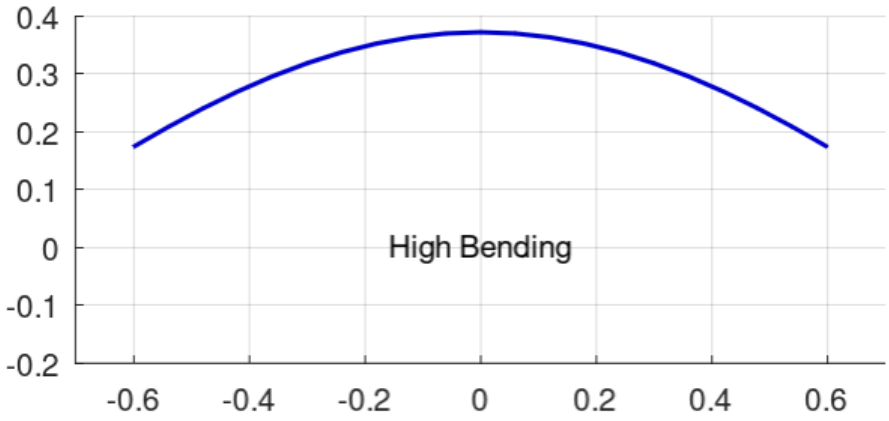

(a) Baseline (n = 0), Efficiency: 9.86×10^{-13}.

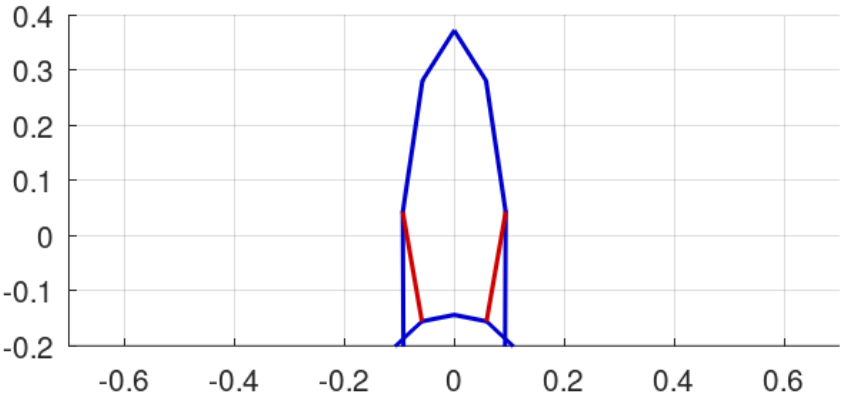

(b) Transitional (n = 4), Efficiency: 3.21×10^{0}.

Figure 4. *Cont.*

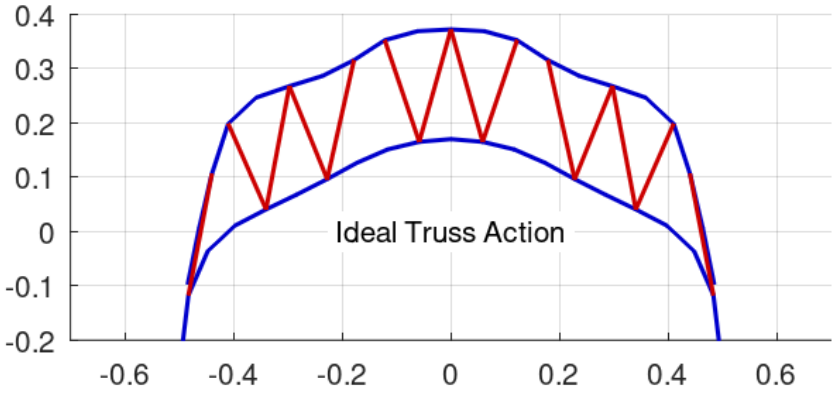

(c) Optimal (n = 14), Efficiency: 4.35 × 10^1.

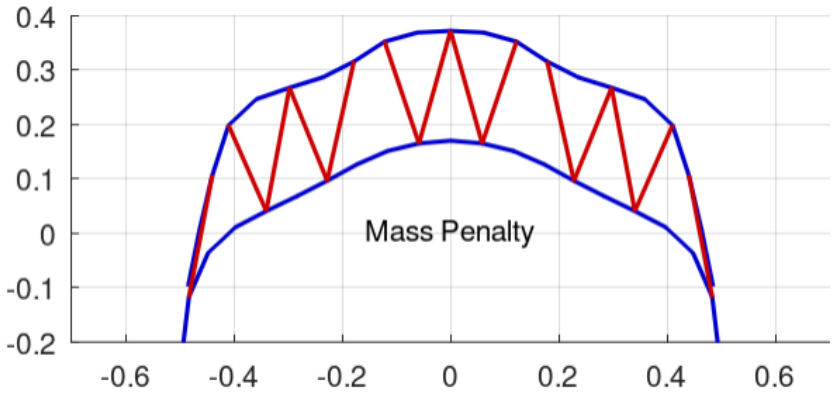

(d) Over-Stiffened (n = 14), Efficiency: 4.35 × 10^1.

Figure 4. Optimal topology development evolution process results of biomimetic lifting beam.

The selection of the optimal biomimetic configuration is quantitatively driven by the multi-objective optimization sweep presented in **Figure 5a–c**, which evaluates the structural response across the entire topological design space (rib counts $n = 0$–14). The fundamental engineering challenge in this design is maximizing the specific stiffness, the ratio of rigidity to mass, without triggering diminishing returns. **Figure 5a** (Stiffness Gain) illustrates a critical threshold in kinematic determinacy. At the baseline state ($n = 0$), the absence of internal shear bracing renders the structure a kinematic mechanism, resulting in a mathematical singularity characterized by catastrophic theoretical deflections (>10^{14} mm). The introduction of a single rib pair ($n = 2$) instantly stabilizes the shell, arresting the Vierendeel frame bending and dropping the deflection by fourteen orders of magnitude. However, **Figure 5b** (Mass Penalty) reveals the inherent cost of this stabilization: the system mass increases strictly linearly as internal members are added, rising from 2.7 kg at the baseline to 4.25 kg at maximum density. The synthesis of these competing parameters is captured in the global objective function plotted in **Figure 5c** (Efficiency). The specific stiffness efficiency curve demonstrates a non-linear sigmoidal growth, transitioning from negligible efficiency at low rib counts to a distinct asymptotic plateau. The global optimum is mathematically identified at the inflection point ($n = 14$), achieving a peak efficiency score of 43.5. Any ribs added beyond this saturation point would incur a direct mass penalty without a proportional reduction in strain energy.

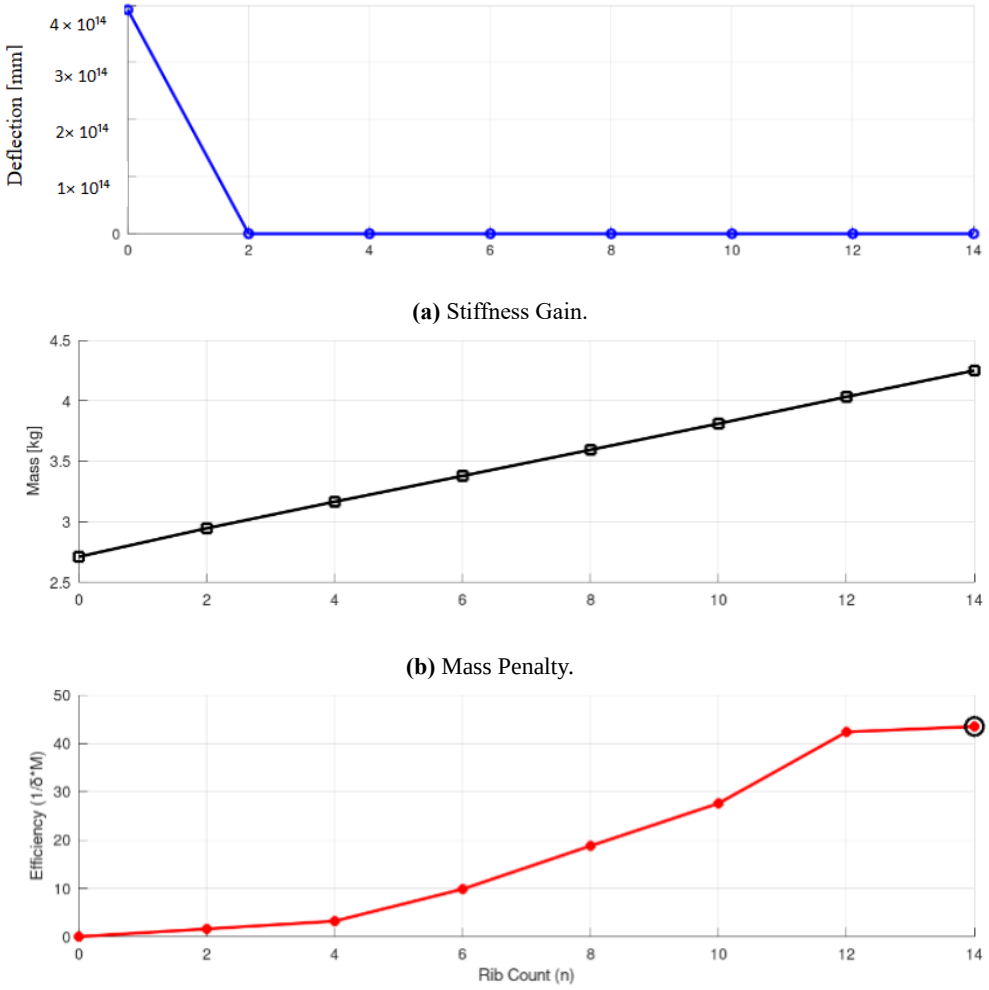

(a) Stiffness Gain.

(b) Mass Penalty.

(c) Global Optimum.

Figure 5. Rib count optimization for: **(a)** Deflection; **(b)** Mass; **(c)** Efficiency.

To rigorously validate the kinematic behavior of this identified optimal state, **Figure 6** presents a high-fidelity relative deformation analysis of the $n = 14$ topology. By overlaying the undeformed reference geometry (dashed black lines) with the deformed operational state (solid blue and red lines, magnified 50×), the illustration explicitly maps the internal force distribution. The global "Arch Action" is immediately evident in the deformation of the blue outer shell: the curvature flattens under vertical loading, thrusting the distal ends outward and successfully converting the primary bending moment into axial compression within the top chord. Crucially, the red internal ribs do not deform uniformly with the shell; rather, they undergo a distinct rigid-body rotation. This tilting mechanism provides definitive kinematic proof of "Shear Coupling." The ribs act as the diagonal struts of a variable-depth truss, rotating to absorb the differential displacement between the upper and lower chords. This geometrically validates the biomimetic hypothesis: the internal dendritic array successfully localizes shear transfer, leaving the graded outer shell optimized strictly for axial and flexural resistance.

The final optimized topology presented in **Figure 4c, Figure 4d** and **Figure 6** manifests as a graded cellular arch frame that morphologically converges with the skeletal architecture of a chiropteran (bat) wing or pterosaurian limb, rather than the typical open-wing structure of an avian species. Unlike a bird wing, which generally relies

on a centralized spar with a lightweight internal trabecular matrix, the optimized beam features a distinct, continuous outer shell that acts as a structural exoskeleton, tapering exponentially from a thick central root to slender tips in a manner analogous to the tapering limb bones of flying mammals. This outer envelope is reinforced by a discrete, zig-zagging network of internal dendritic ribs that resembles a variable-depth Warren truss or the elongated phalanges supporting a membrane. This geometric configuration creates a highly efficient voided lattice where the curved upper and lower chords manage the primary bending moments through arch action, while the internal diagonal ribs provide the necessary shear bracing, thereby synthesizing the lightweight efficiency of biological venation with the kinematic stability of engineered truss systems.

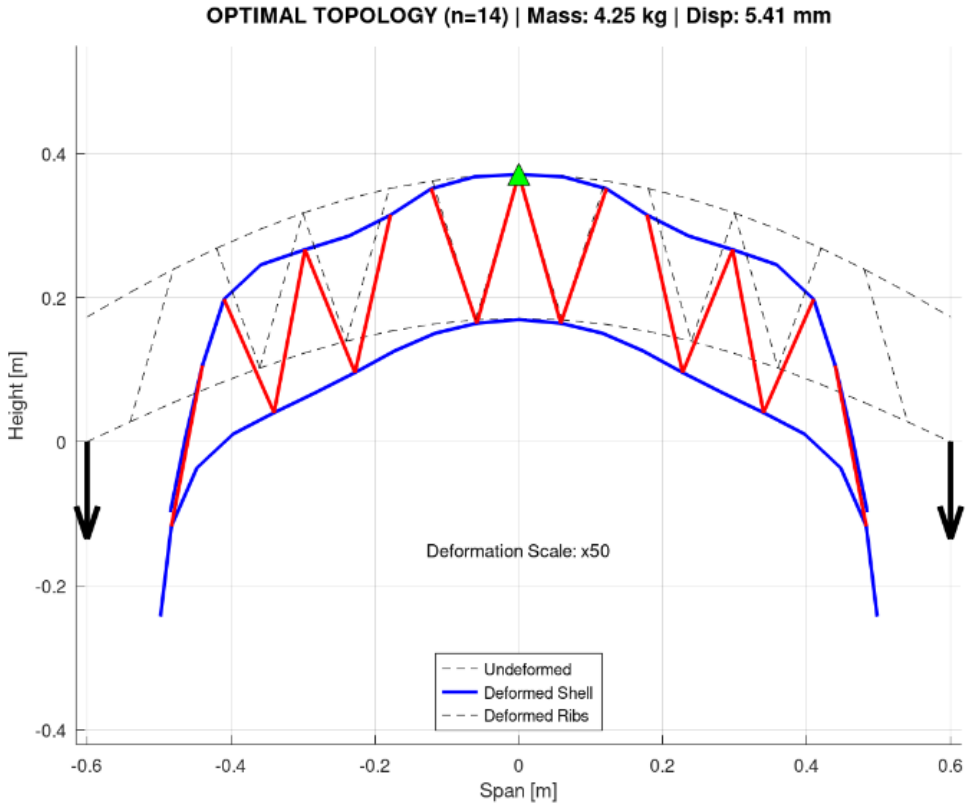

Figure 6. Optimal topology results of biomimetic lifting beam.

7. Discussion: Structural analogy with bicycle brake mechanisms

An intriguing structural parallel can be drawn between the proposed biomimetic lifting beam and high-performance mechanical braking systems employed in cycling, specifically V-brakes and cantilever calipers. While ostensibly serving different functions, one static load-bearing and the other dynamic friction-actuation. These systems share fundamental architectural principles regarding arch action, stiffness-to-weight optimization, and shear flow management.

Both configurations utilize an arched or U-shaped caliper structure that transmits force from the rim (or hook) through dual arms converging at a central anchor point. This arrangement facilitates the transfer of loads via optimized geometries, distributing both tensile and compressive forces across the system. Similarly, the bio-inspired lifting beam employs a graded shell and a network of internal ribs to redirect bending moments

efficiently through a hierarchical and symmetric structure:

(i) **Arch action and load path redirection:** In V-brake systems, the arched caliper inherently channels braking forces into the fork or frame boss, thereby optimizing the transmission of load into a central supporting structure. Analogously, the lifting beam's arch-like form concentrates vertical loads into the central lifting eye, creating a direct and efficient load path. In both cases, the design philosophy emphasizes stiffness through geometrical curvature and strategic material placement, minimizing structural weight without compromising performance.

(ii) **Material grading and compliance tuning:** Bicycle brake arms often feature tapered profiles or machined cutouts to regulate stiffness and dynamic response. This mechanical tailoring is conceptually analogous to the exponential thickness grading $t(x)$ implemented in the lifting beam. The taper parameter α, introduced in Section 2, mirrors the gradual sectional variation in brake arms, effectively compensating for local stress gradients and ensuring more uniform compliance under external loading.

(iii) **Redundancy and structural safety:** Redundancy is an essential safety feature in dual-arm caliper systems, enabling continued functionality even if one arm is damaged or fatigued. A comparable strategy is embedded in the lifting beam's design via the inclusion of multiple internal ribs (n ribs), which form a distributed and redundant load-bearing network. This configuration enhances fault tolerance: the failure of an individual rib does not precipitate catastrophic structural compromise, thereby supporting fail-safe operation.

These structural analogies reinforce the engineering validity and practical feasibility of the proposed bio-inspired topology. The arch-and-arm geometry, the principle of graded compliance, and the strategic use of redundancy are all well-established in cycling technology, where they have demonstrated durable, high-performance behavior under repeated stress cycles. Consequently, future experimental validation of the lifting beam could benefit from adopting established testing protocols, such as ISO 4210 fatigue tests for bicycle components, as a standardized basis for assessing cyclic durability, material fatigue, and operational safety.

7.1. Geometric homology and arch action

Both configurations utilize an arched or U-shaped caliper structure to transmit forces from distal points (hooks or brake pads) to a central pivot (lifting eye or frame boss). In V-brake systems, the arched caliper inherently channels the braking reaction forces into the fork via compression, utilizing the geometry to minimize flex. Analogously, the FEA results (**Figure 3**) confirm that the lifting beam's arched profile converts vertical hoisting loads into axial compressive flux along the upper chord. This geometric homology validates the efficiency of the "arch-and-arm" morphology: by aligning material with the principal compressive stress trajectories, both systems minimize the reliance on inefficient bending resistance, thereby maximizing specific stiffness.

The analogy to bicycle V-brakes requires nuance. While brake arms undergo

significant out-of-plane torque during actuation, lifting beams are dominated by in-plane bending. However, the geometric homology remains valid: both systems utilize an arch to convert bending moments into compressive flows toward a central pivot (or lifting eye). The biomimetic ribs act similarly to the truss-like cutouts often CNC-machined into high-end brake arms to maximize specific stiffness.

7.2. On safety factors and code compliance

Heavy lifting devices are safety-critical and subject to regulatory scrutiny. While topology optimization and biomimetic geometries can reduce mass, conservative design margins and proof testing are mandatory. It is recommended to use initial safety factors consistent with API/ASME crane standards (e.g., design factor ≥ 5 for lifting lug components until proven by fatigue testing).

7.3. The truss effect and shear decoupling

The most critical convergence lies in the role of internal voiding. High-end brake calipers often feature CNC-machined triangular cutouts or "trussing" to reduce mass without compromising braking power. Our numerical sensitivity analysis (Section 6.1) reveals that the internal dendritic ribs in the lifting beam perform an identical mechanical function. The FEA proved that these ribs do not merely reduce weight; they actively carry shear loads via axial tension/compression, preventing the "lozenging" or shear deformation of the frame. This mirrors the design logic of skeletonized brake arms, where internal cross-bracing prevents the arm from twisting or collapsing under cable tension. The beam's ribs "decouple" the shear stress from the outer shell (**Figure 3c**), just as brake arm trusses decouple the actuation force from the arm's bending compliance, ensuring a crisp, responsive transfer of force.

7.4. Planar vs. torsional loading nuance

While the geometric analogy is robust, a distinction in loading conditions must be acknowledged. Bicycle brake arms are subjected to significant out-of-plane torque (twisting) during actuation due to the offset between the pad and the pivot. In contrast, the lifting beam is dominated by in-plane bending and shear. However, the biomimetic solution addresses this through the graded thickness parameter $t(x)$. Just as brake arms are tapered to be thickest at the pivot to resist torsion, the lifting beam is exponentially thickened at the central eyelet to resist the peak bending moment. Thus, while the load vectors differ (torsion vs. bending), the morphological response, tapering material toward the root—remains a universal constant in structurally optimized design.

7.5. Redundancy and fail-safe operation

Finally, the concept of distributed redundancy is central to both systems. In a dual-arm caliper, the failure of one side compromises the system but does not result in immediate catastrophic detachment. Similarly, the dendritic rib network ($n = 6$) provides a redundant load path. If a single rib were to yield or fracture due to a manufacturing defect, the load would redistribute through the adjacent truss members and the shell, preventing the immediate collapse mechanism associated with monolithic

single-load-path structures. This fault tolerance is a hallmark of biological structures and a critical requirement for safety-critical lifting hardware.

7.6. Manufacturability and scalability

Additive manufacturing allows complex internal topologies, but build volume and economics are constraints for large industrial beams. Hybrid approaches (AM joints with predominantly conventional machined members, or segmented AM shells) and topology simplification for large scale are discussed. For aerospace minimum mass is paramount; AM is appropriate. For heavy-industry crane beams, segmented or hybrid manufacturing may be more practical.

7.7. Limitations

Analytical model approximations (thin-plate shell inertia approximations, simplified rib centroid positions) produce conservative but not exact predictions. Finite element models (3D solid) are necessary for final design. Material anisotropy and defects in AM parts reduce effective □ and fatigue life; these require experimental calibration. Stress concentration at rib roots and eye/hook interfaces must be carefully filleted in final designs.

7.8. Applications and potential impact

Applications include:

(i) **Industrial lifting and cranes:** lighter lifting beams reduce crane deadweight and increase net payload.
(ii) **Modular and temporary construction:** rapid assemblies with lighter rigging.
(iii) **Aerospace ground support and payload handling:** high specific stiffness favorable to mass-critical operations.
(iv) **Marine salvage:** corrosion-resistant alloys and optimized buoyancy for underwater applications.

For each application the design must be adapted for scale, load cases, environmental conditions (corrosion, temperature), and regulations.

8. Conclusion

This manuscript has proposed and thoroughly analysed a biomimetic lifting-beam topology that unites an exponentially graded outer shell with an internal, dendritic rib network to realise high specific stiffness at constrained mass. Using a structured, multi-fidelity modelling chain variable-section Euler–Bernoulli theory for expedient preliminary sizing, Timoshenko shear-corrected beam theory for "deep-beam" behaviour, and a discrete 2D arch-frame finite element model for full kinematic and local stress fidelity, we have quantified both the global advantages and the critical local failure modes of the proposed architecture. The principal conclusions from the analytical and numerical investigations are as follows.

First, graded thickness and rib placement that align with principal stress trajectories materially improve section modulus and reduce global bending demands: parametric

comparisons indicate that, for representative baseline geometries and material properties, reallocating material to the central region and introducing a moderate number of ribs produces roughly a 15–25% improvement in performance metrics (≈20% reduction in peak bending stress and ≈15% reduction in midspan deflection at equal mass relative to traditional solid sections). These improvements arise because the graded shell carries bending efficiently while the ribs convert vertical shear into axial ribs forces, thereby activating truss-like load paths (the "Truss Effect").

Second, shear effects are non-negligible for the considered span-to-depth ratios. For relatively shallow slenderness (e.g., $\lambda \approx 3.4$ in the study), the shear component contributes on the order of 20–25% of the total deflection; neglecting shear (Euler–Bernoulli assumptions) underestimates compliance and can produce non-conservative serviceability predictions. Incorporation of a Timoshenko correction is therefore mandatory when designing ribbed, open-web, or highly porous lifting geometries.

Third, multi-fidelity comparison demonstrates that analytical, "smeared" continuum models systematically underpredict local stress concentrations inherent to discrete rib–shell junctions. The 2D FEA captures jagged, saw-tooth stress profiles where rib members interface with the shell; peak local stresses exceed the analytical mean by ≈60% in our cases, creating fatigue-critical hot spots. Consequently, any practical implementation must include local geometric refinement (fillets, material continuity), AM process control to limit defects, and fatigue-oriented design margins.

Fourth, the topology exhibits three behavioral regimes as rib density increases: an initial unstable Vierendeel-like state (insufficient ribs), a favourable truss regime (moderate ribs, large specific-stiffness gains), and a solid-web regime (high rib density with negligible stiffness gain per mass added). For the baseline parameter set the truss regime (approximately 4–7 ribs in the symmetric layout) yields the best trade-off between stiffness and mass; further densification enters diminishing returns and is inadvisable for mass-sensitive applications. The obtained optimal shape is technically a Variable-Depth Arched Truss. However, visually, it evokes the skeletal framework of a bat's wing due to the combination of a tapered "limb" (the shell) reinforced by thin, diagonal "bones" (the ribs).

Fifth, manufacturability constraints and uncertainty are decisive design drivers. Additive manufacturing enables realization of the required geometry, but imposes minimum feature sizes, overhang and residual-stress constraints, and variable effective mechanical properties. A conservative knock-down to effective modulus and explicit uncertainty quantification (FOSM approximations used here) show variability bands of the order of ±6–10% for stress and deflection under typical AM tolerances and material scatter; embedding reliability-aware surrogates and probabilistic constraints into the topology workflow is therefore necessary for certification of lifting hardware.

Taken together, these conclusions establish that the proposed biomimetic topology is a viable route to lighter, stiffer lifting beams provided that: (i) designers account for shear through Timoshenko or higher-fidelity models in sizing; (ii) local stress risers at rib junctions are mitigated by fillets and detail design; (iii) AM process variability is quantified and controlled; and (iv) optimization is extended to include

probabilistic/fatigue objectives and manufacturability constraints. The manuscript provides a concrete validation program (prototype AM fabrication, DIC full-field strain mapping, static and fatigue testing, NDT/CT inspection) that, if executed, will enable direct verification of the analytical predictions and support transition of the concept to certified use.

Finally, while the present work focused on in-plane bending/shear behaviour and static/fatigue performance, future efforts should integrate surrogate-based reliability approaches (e.g., robust-weighted hybrid regression) and single-loop multidisciplinary optimization to co-optimize stiffness, fatigue life and manufacturing process parameters under multi-source uncertainties, thereby, producing lifting beams that are not only efficient, but demonstrably robust under real-world variability. The full set of analyses and design rules summarized here (and in the accompanying manuscript) provide a practical roadmap for turning the biomimetic lifting-beam concept into deployable engineering hardware.

Supplementary materials: The full OCTAVE code can be downloaded at: https://ojs.acad-pub.com/public/MEA-3582-Supplemantry-Material-Code.txt.

Funding: This research has no funding source.

Institutional review board statement: Not applicable.

Informed consent statement: Not applicable.

Data availability statement: The full OCTAVE code is available separately in the **Supplementary materials**.

Conflict of interest: The author declares that he has no conflict of interest.

References

1. Sarikaya M. An introduction to biomimetics: A structural viewpoint. Microscopy Research and Technique. 1994; 27(5): 360–375.
2. Waggoner MC, Kestner D. Biomimicry and structural design: Past, present, and future. In Structures Congress 2010. American Society of Civil Engineers; 2010. pp. 2852–2863.
3. Joshy R. Biomimetics in structural design. International Journal of Scientific Research. 2017; 7(12): 132–141.
4. Tang PS, Chang KH. Integration of topology and shape optimization for design of structural components. Structural and Multidisciplinary Optimization. 2001; 22(1): 65–82.
5. Wu J, Clausen A, Sigmund O. Minimum compliance topology optimization of shell–infill composites for additive manufacturing. Computer Methods in Applied Mechanics and Engineering. 2017; 326: 358–375.
6. Oh S, Jung Y, Kim S, et al. Deep generative design: integration of topology optimization and generative models. Journal of Mechanical Design. 2019; 141(11): 111405. doi: 10.1115/1.4044229
7. Watson M, Leary M, Brandt M. Generative design of truss systems by the integration of topology and shape optimisation. The International Journal of Advanced Manufacturing Technology. 2022; 118(3): 1165–1182.
8. Hooshmand A, Campbell MI. Truss layout design and optimization using a generative synthesis approach. Computers and Structures. 2016; 163: 1–28.
9. Thomas S, Li Q, Steven G. Topology optimization for periodic multi-component structures with stiffness and frequency criteria. Structural and Multidisciplinary Optimization. 2020; 61(6): 2271–2289.
10. Oliver J, Yago D, Cante J, et al. Variational approach to relaxed topological optimization: Closed form solutions for

structural problems in a sequential pseudo-time framework. Computer Methods in Applied Mechanics and Engineering. 2019; 355: 779–819.
11. Siddique SH, Hazell PJ, Pereira GG, et al. On the mechanical behaviour of biomimetic cornstalk-inspired lightweight structures. Biomimetics. 2023; 8(1): 92.
12. Röver T, Fuchs C, Asami K, et al. Dimensioning of biomimetic beams under bending for additively manufactured structural components. Biomimetics. 2024; 9(4): 214.
13. Gandhi Y, Minak G. A review on topology optimization strategies for additively manufactured continuous fiber-reinforced composite structures. Applied Sciences. 2022; 12(21): 11211.
14. Mehboob A, Barsoum I, Mehboob H, et al. Topology optimization and biomechanical evaluation of bone plates for tibial bone fractures considering bone healing. Virtual and Physical Prototyping. 2024; 19(1): e2391475.
15. Tian M, Liu Y, Chen Z, et al. Biomimetic design and validation of an adaptive cable-driven elbow exoskeleton inspired by the shrimp shell. Biomimetics. 2025; 10(5): 271.
16. Dixit S, Stefańska A. Bio-logic, a review on the biomimetic application in architectural and structural design. Ain Shams Engineering Journal. 2023; 14(1): 101822.
17. Hassan HZ, Saeed NM. Advancements and applications of lightweight structures: a comprehensive review. Discover Civil Engineering. 2024; 1(1): 47.
18. Zhang H, Yang H, Yang Y, et al. Gust response and alleviation of avian-inspired in-plane folding wings. Biomimetics. 2024; 9(10): 641.
19. Shiokawa Y, Liu R, Sawada H. A biomimetic flapping mechanism for insect robots driven by indirect flight muscles. Biomimetics. 2025; 10(5): 300.
20. Morales EDC. Comparative Analysis of Generative Design and Topology Optimization in Mechanical Component Development [PhD Thesis]. Purdue University; 2025.
21. Wolff J. The Law of Bone Remodelling. Springer; 1986.
22. Ashby MF, Gibson LJ. Cellular Solids: Structure and Properties. Cambridge University Press; 1997.
23. Gao H, Ji B, Jäger IL, et al. Materials become insensitive to flaws at nanoscale: lessons from nature. Proceedings of the National Academy of Sciences. 2003; 100(10): 5597–5600.
24. Mattheck C. Design in Nature: Learning from Trees. Springer; 1998.
25. Bendsøe MP, Sigmund O. Topology Optimization: Theory, Methods, and Applications. Springer Science and Business Media; 2004.
26. Guest JK, Prévost JH. Topology optimization of creeping fluid flows using a Darcy–Stokes finite element formulation. International Journal for Numerical Methods in Engineering. 2006; 66(3): 461–484.
27. Stampfl J, Pettermann HE, Liska R, et al. Bioinspired cellular structures: Additive manufacturing and mechanical properties. In: Gruber P, Bruckner D, Hellmich C, et al. (editors). Biomimetics—Materials, Structures and Processes. Springer; 2011. pp. 105–123.
28. Yang S, Meng D, Alfouneh M, et al. A robust-weighted hybrid nonlinear regression for reliability based topology optimization with multi-source uncertainties. Computer Methods in Applied Mechanics and Engineering. 2025; 447: 118360.
29. Meng D, Zhu SP. Multidisciplinary Design Optimization of Complex Structures under Uncertainty. CRC Press; 2024.
30. Timoshenko SP. LXVI. *On the correction for shear of the differential equation for transverse vibrations of prismatic bars*. The London, Edinburgh, and Dublin Philosophical Magazine and Journal of Science. 1921; 41(245): 744–746.